NANO: Brief Reports and Reviews
Vol. 5, No. 3 (2010) 175–184

DOI: 10.1142/S1793292010002086

World Scientific
www.worldscientific.com

# FORMATION OF NANOLITER BUBBLES IN MICROFLUIDIC T-JUNCTIONS

JING FAN, YUXIANG ZHANG and LIQIU WANG*
*Department of Mechanical Engineering*
*The University of Hong Kong*
*Pokfulam Road, Hong Kong*
**lqwang@hku.hk*

Received 15 December 2009
Accepted 14 April 2010

A numerical study on nanoliter bubble formation process in microfluidic T-junctions is conducted. The simulated bubble sequence agrees well with experiments. The pressure and velocity distribution in liquid phase, and streamlines of relative velocity of liquid to bubbles are obtained. We also studied pressure variation at the junction and gas flow rate for the first several bubbles, and illustrated the special impact of channel width ratio on bubble formation process. Finally, we derived the critical nondimensional gas pressure above which bubbles can be generated.

*Keywords*: Microfluidic T-junction; nanoliter bubble formation; two-phase flow; numerical simulation.

## 1. Introduction

Generation of nanoliter bubbles is an elementary function of many microfluidic systems because of its wide range of applications, particularly when the bubble size is uniform. Examples include chemistry, biochemistry, biomedical engineering, chemical engineering, food industry, pharmaceuticals, foams, material sciences, microelectronics, lab-on-a-chip, microfluidic chips, micromixers, micropower generation, microreactors and micrototal analysis systems ($\mu$ TAS).[1–14] Their fundamental medical applications range from ultrasound contrast agents for noninvasively imaging both the "macrovascular" anatomy and more importantly, the "microvascular" physiology, to therapeutic delivery systems for delivering site-specific therapy to targeted organs in the body and as the carriers for newer therapeutic options.[13,14] In addition, intravenous injection of a stabilized solution of sufficiently small bubbles might be used in acute lung disfunction.[4] The size and its distribution are critical in all these applications. Conventional techniques generate bubbles by the chaotic interactions of surface tension, viscosity and turbulence, usually involving complex machinery or chemical reactions.[1–3] Little control over the formation of individual bubbles is available, and a broad distribution of sizes is typically produced.[1–3]

In an attempt to produce highly controllable nanoliter-bubbles with size distributions significantly more narrow than those generated using conventional methods, a "bottom-up" approach — microfluidic T-junction — has been recently proposed for fabricating bubbles at the level of individual bubbles.[15–18] In the approach, the bubble is formed at the T-junction of two microfluidic channels conveying a gas and a liquid into the junction respectively. The approach operates in the laminar flow region and generates one

*Corresponding author.

bubble at a time at the T-junction. As the conditions for the generation are identical for every bubble, the bubbles generated by this approach are highly monodispersed, with a coefficient of variation (CV) of the bubble diameter less than 2%.[15–18] Here CV is defined by CV $= \sigma_d/d_m$ where $\sigma_d$ is the standard derivation of the diameter and $d_m$ is its mean value. In particular, for fixed fluid properties and geometry, there exists a range where the bubble generation frequency depends only on liquid inlet pressure but not on the gas pressure.[18] This offers the advantage of generating different-sized bubbles at a fixed frequency by varying the gas pressure. The approach also provides a simple means of enhanced mixing in liquid slugs separated by discrete gas bubbles generated at the T-junction due to both the reduction of the diffusion length and the internal recirculation within the slugs.[19,20]

The present work aims to further develop this promising technique by simulating the bubble formation process in microfluidic T-junctions numerically. The numerical scheme is based on the finite-element method encoded in MATLAB with equation solver COMSOL. The used front-tracking method can capture the gas–liquid interface more accurately than the front-capturing methods commonly used in literature.[21–23] The present work is the first attempt to simulate the gas–liquid flow in T-junctions by this method although it was once applied for flow-focusing device.[24,25] We will study the bubble formation process, pressure and velocity distributions, relative velocity streamlines, pressure variation at the junction and gas flow rate. In addition, we will analyze the impact of channel width ratio on bubble formation process and find the condition for generating the most bubbles for the specified volume of two-phase fluid. Finally, based on numerical simulation and experimental observation, we determine a critical value of non-dimensional gas pressure above which bubbles can be generated.

## 2. Governing Equations and Numerical Algorithm

Consider a two-dimensional T-junction as illustrated in Fig. 1. A liquid stream (grey-colored) flows into the T-junction from the left inlet of main channel, while a gas stream (white-colored) flows into the T-junction from the vertical gas channel under constant pressure $p_g$. The two streams then meet at the junction. For a certain range of flow parameters, the gas breaks periodically to form bubbles which then flow downstream to the right outlet of the main channel.

For this system, the spatial characteristic dimensions are the widths of gas channel and main channel which are marked as $D_1$ and $D_2$ in Fig. 1. Compared with the liquid, the gas viscosity and density are negligibly small. The gas pressure variation is also relatively small so that we can specify a constant pressure for the whole gas domain.[24] Thus the liquid–gas interface is regarded as a boundary of the liquid phase, on which Young–Laplace equation

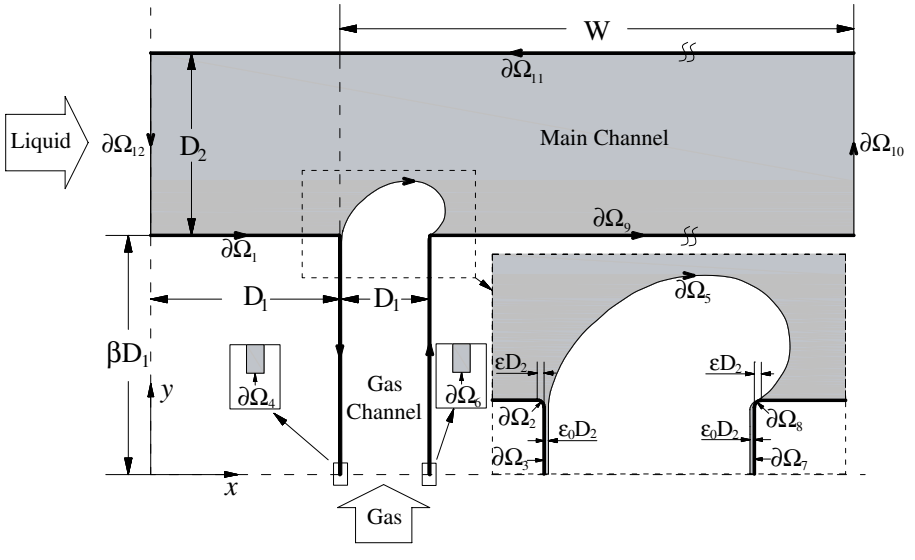


Fig. 1. Sketch of two-dimensional microfluidic T-junction with all relevant lengths shown.

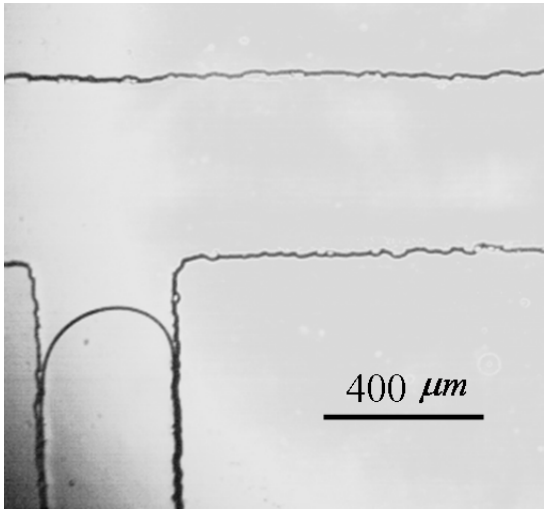


Fig. 2. Snapshot of gas tip shape in experiments.[18]

is fulfilled. Because experiments show a thin liquid film between the gas stream and the solid wall of gas channel (Fig. 2) which may result from the poor wettability of gas with wall, we also keep such a film in our simulations (Fig. 1).

For the two-dimensional Cartesian coordinate system $(x, y)$ in Fig. 1, the Navier–Stokes and continuity equations for incompressible Newtonian liquid in terms of nondimensional variables, can be written as

$$\begin{bmatrix} \mathrm{Re}\dfrac{\partial\tilde{u}}{\partial\tilde{t}} \\ \mathrm{Re}\dfrac{\partial\tilde{v}}{\partial\tilde{t}} \\ 0 \end{bmatrix} + \tilde{\nabla}\cdot\begin{bmatrix} \left(2\dfrac{\partial\tilde{u}}{\partial\tilde{x}}-\tilde{p}\right) & \left(\dfrac{\partial\tilde{u}}{\partial\tilde{y}}+\dfrac{\partial\tilde{v}}{\partial\tilde{x}}\right) \\ \left(\dfrac{\partial\tilde{u}}{\partial\tilde{y}}+\dfrac{\partial\tilde{v}}{\partial\tilde{x}}\right) & \left(2\dfrac{\partial\tilde{v}}{\partial\tilde{y}}-\tilde{p}\right) \\ 0 & 0 \end{bmatrix} = \begin{bmatrix} \mathrm{Re}\left(\dfrac{\partial\tilde{u}}{\partial\tilde{t}}+\tilde{u}\dfrac{\partial\tilde{u}}{\partial\tilde{x}}+\tilde{v}\dfrac{\partial\tilde{u}}{\partial\tilde{y}}\right) \\ \mathrm{Re}\left(\dfrac{\partial\tilde{v}}{\partial\tilde{t}}+\tilde{u}\dfrac{\partial\tilde{v}}{\partial\tilde{x}}+\tilde{v}\dfrac{\partial\tilde{v}}{\partial\tilde{y}}\right) \\ \dfrac{\partial\tilde{u}}{\partial\tilde{x}}+\dfrac{\partial\tilde{v}}{\partial\tilde{y}} \end{bmatrix}, \tag{1}$$

where $\tilde{\nabla} = (\partial/\partial\tilde{x}, \partial/\partial\tilde{y})$, and the tilde $(\tilde{})$ identifies nondimensional parameters. Here,

$$\tilde{x} = \frac{x}{D_2}, \quad \tilde{y} = \frac{y}{D_2}, \quad \tilde{u} = \frac{u}{u_{\mathrm{in}}}, \quad \tilde{v} = \frac{v}{u_{\mathrm{in}}},$$
$$\tilde{t} = \frac{t}{D_2/u_{\mathrm{in}}}, \quad \tilde{p} = \frac{p}{\mu u_{\mathrm{in}}/D_2}, \quad \mathrm{Re} = \frac{\rho u_{\mathrm{in}} D_2}{\mu}, \tag{2}$$

where $u$ and $v$ are the velocity components in $x$ and $y$ directions, respectively. $u_{\mathrm{in}}$ is the mean liquid velocity at the inlet, $t$ is the time, $p$ is the liquid pressure. $\mu$ and $\rho$ are the liquid viscosity and density, respectively.

In microfluidic systems, the liquid velocity is usually on the order of $10^{-3} - 10^{-2}$ m/s. The characteristic dimension of microchannels is about tens of micrometers. Taking water as the sample liquid, the Reynolds number Re in microfluidic systems is on the order of $10^{-2} - 10^{-1}$. The flow can thus be regarded as Stokes flow. Equation (1) simplifies to the Stokes equation:

$$\tilde{\nabla}\cdot\begin{bmatrix} \left(2\dfrac{\partial\tilde{u}}{\partial\tilde{x}}-\tilde{p}\right) & \left(\dfrac{\partial\tilde{u}}{\partial\tilde{y}}+\dfrac{\partial\tilde{v}}{\partial\tilde{x}}\right) \\ \left(\dfrac{\partial\tilde{u}}{\partial\tilde{y}}+\dfrac{\partial\tilde{v}}{\partial\tilde{x}}\right) & \left(2\dfrac{\partial\tilde{v}}{\partial\tilde{y}}-\tilde{p}\right) \\ 0 & 0 \end{bmatrix} = \begin{bmatrix} 0 \\ 0 \\ \dfrac{\partial\tilde{u}}{\partial\tilde{x}}+\dfrac{\partial\tilde{v}}{\partial\tilde{y}} \end{bmatrix}. \tag{3}$$

Young–Laplace equation is applied as the dynamic boundary condition on the interface $\partial\Omega_5$:

$$n_j\tilde{\sigma}_{ij} = -\left(\tilde{p}_g + \frac{1}{Ca}\tilde{\kappa}\right)n_i\,. \tag{4}$$

Here $\mathbf{n} = (n_x, n_y)$ is the unit normal of the interface in the $xy$ plane, $\tilde{\sigma}_{ij}$ is the nondimensional stress tensor defined by $\sigma_{ij}/(\mu u_{\mathrm{in}}/D_2)$ with $\sigma_{ij}$ as the stress tensor. $\tilde{p}_g$ is the nondimensional gas pressure and $Ca$ is the capillary number. $\tilde{\kappa}$ is the mean curvature of the interface. They are defined by

$$\tilde{p}_g = \frac{p_g}{\mu u_{\mathrm{in}}/D_2}\,, \tag{5}$$

$$Ca = \frac{\mu u_{\mathrm{in}}}{\gamma}\,, \tag{6}$$

$$\tilde{\kappa} = \frac{\tilde{y}''\tilde{x}' - \tilde{x}''\tilde{y}'}{(\tilde{x}'^2 + \tilde{y}'^2)^{3/2}}\,, \tag{7}$$

where $p_g$ is the gas pressure and $\gamma$ is the surface tension. Here the interface is represented by a parametric curve $\tilde{\boldsymbol{\chi}}(S) = [\tilde{x}(S), \tilde{y}(S)]$, where $S$ is the arc-length scaled by the total length of interface. Single prime $(')$ and double primes $('')$ in Eq. (7) represent first and second derivatives with respect to $S$, respectively.

The following kinematic boundary condition is used to update the interface location:

$$\frac{d\tilde{\boldsymbol{\chi}}}{d\tilde{t}} = \tilde{\mathbf{u}}(\tilde{\boldsymbol{\chi}})|_{\tilde{\boldsymbol{\chi}}\in\partial\Omega_i}\,. \tag{8}$$

We use the second-order Runge–Kutta scheme for resolving this equation.

Other boundary conditions include:

$$\tilde{u} = -6[\tilde{y}^2 - (2\beta+1)\tilde{y} + \beta(\beta+1)], \quad \tilde{v} = 0 \text{ on the inlet boundary: } \partial\Omega_{12}\,, \tag{9a}$$

$$\tilde{p} = 0 \text{ on the outlet boundary: } \partial\Omega_{10}\,, \tag{9b}$$

$$\tilde{u} = \tilde{v} = 0 \text{ on channel walls: } \partial\Omega_{1,2,3,4,6,7,8,9,11}\,. \tag{9c}$$

Here, $\beta$ is a nondimensional length scaling factor as shown in Fig. 1, denoting the ratio between the length and width of the gas channel. The geometric definitions of all boundaries are illustrated in Fig. 1, where the boundaries $\partial\Omega_2$ and $\partial\Omega_8$ are two round corners with a radius of $\varepsilon$. Equations (3), (4), (8)–(9c) define a mathematical model that fully describes the bubble formation process.

In experiments, a semicircle-shaped gas tip is observed in the gas channel before a bubble forming (Fig. 2). Thus, we use a semicircle tip for the initial shape of gas–liquid interface. At each time step, the velocity field is obtained by solving the governing equation, Eq. (3), for specified interface shape at that time instant. Then the interface is assumed to move at the same speed of the liquid particle next to it and is updated by using the kinematic boundary condition, Eq. (8). The velocity field can thus be resolved again for the new interface location. This process is repeated until a bubble breaks up.

A second-order Runge–Kutta scheme coded in MATLAB is used to advance the interface. The finite-element solver COMSOL interfaces with MATLAB to resolve the velocity and pressure fields of liquid at each time instant. The mesh is generated based on the Delaunay algorithm.[26] The initial number of nodes at the interface is set to be 80. Since the computational domain is remeshed at each time step, this number increases to several hundreds when a bubble forms. The element size at the interface is set to be not larger than 0.03. There are a total of several thousand elements for the whole computational domain. This mesh is proved to be fine enough to obtain grid-independent solution.[24] When the governing equation is solved by COMSOL, it is transformed to its variational form based on the variational principle. Variational equations are then solved by an affine invariant form of the damped Newton method.[26] The criterion of convergence is that the weighted Euclidean norm $((1/N)\sum_i(|E_i|/W_i)^2)^{1/2}$ is less than $10^{-6}$ ($N$ is the number of degrees of freedom, $E_i$ is the estimated error in true solution vector, and $W_i$ is the weight factor). The validity of the code for simulating two-phase problems has been well assessed. Readers are referred to Ref. 24 for the details. In order to simulate the interface evolution after a bubble breaking up, a small length scale $\delta_0$ (0.01) is defined to determine when to break the gas thread. When the vertical distance $\delta$ from the corner ($\partial\Omega_8$) to the interface (shown in Fig. 3) is less than $\delta_0$, we use two arcs to cap the new bubble and gas thread. The radiuses of the two arcs are adjusted to approximate $\delta_0$ for each case. Unless $\delta_0$ is too small to be annihilated by the spatial resolution, this method can deal with the break-up phenomenon effectively without influencing the overall dynamic of the system.

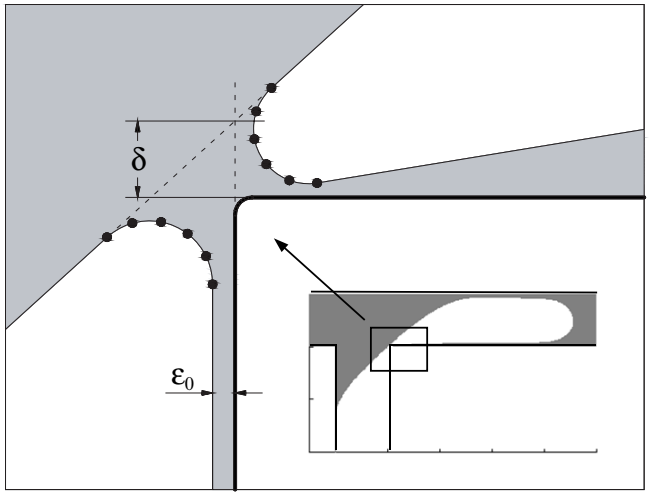


Fig. 3. Sketch on the bubble break-up implementation.

The ideal gas law is applied to bubbles which have broken away from the gas stream. The product of bubble volume and absolute pressure is thus constant. In this study, the atmospheric pressure is set about ten times of the superficial pressure of gas phase. Thus the variation of bubble size from the junction to the outlet is within 10%.

Figure 4 compares the simulated bubble growth morphology with that from experiments, showing a good agreement between the two.

## 3. Results and Discussion

### 3.1. *Bubble sequence*

We simulate the bubble formation process at $\tilde{D}_1 = 1$, $\tilde{W} = 40$, $\tilde{p}_g = 900$, and $Ca = 0.03$. The simulation snapshot of a six-bubble sequence is illustrated in Fig. 5. In this 2-D system, the area of each bubble is used to characterize the bubble size. The sizes

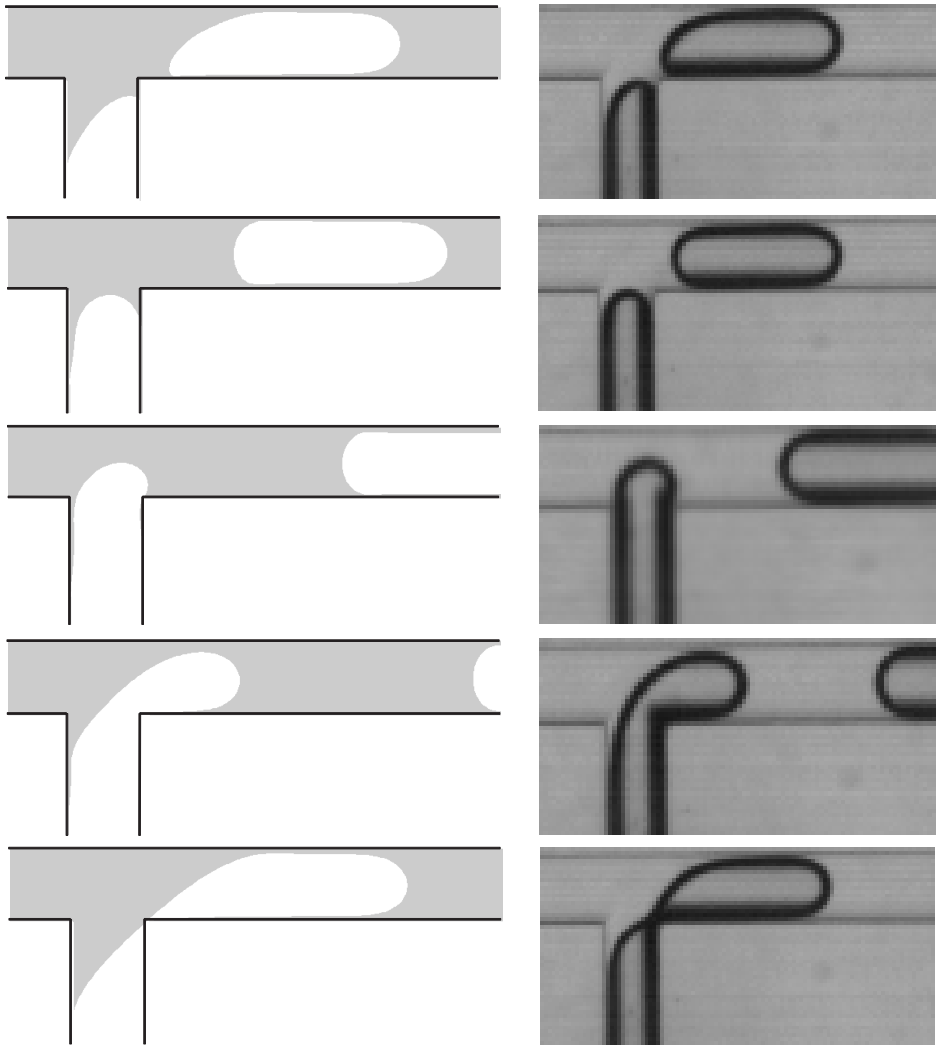

(a) (b)

Fig. 4. Bubble growth morphology: (a) simulation results and (b) snapshots from experiments[17] ($\tilde{D}_1 = 1$, $\tilde{W} = 40$, $\tilde{p}_g = 900$, and $Ca = 0.03$).

of the first six bubbles under the same pressure as in gas channel are 2.31, 2.35, 2.40, 2.47, 2.53 and 2.60, respectively.

Figure 6 illustrates the pressure distribution in liquid phase along the centerline of the main channel. The absolute velocity field is illustrated in Fig. 7, where arrows indicate the flow direction and different colors indicate the magnitude of velocity. Both pressure and velocity distributions show that the flow in liquid slugs between bubbles is Poiseuille flow (except the regions very near to bubbles). Moreover, streamlines of relative velocity in liquid slugs are illustrated in Fig. 8. Here the relative velocity is defined as:

$$\tilde{u}_r = \tilde{u} - \tilde{u}_b \,, \tag{10}$$

where $\tilde{u}_b$ is the nondimensional bubble velocity. Simulation shows that all bubbles flow at the same velocity, $\tilde{u}_b$ is thus calculated by dividing the centroid position change of one bubble ($\Delta\tilde{x}$) by the time period ($\Delta\tilde{t}$). Vortexes are observed in the relative velocity field, which indicates a better mixing of liquid near bubble caps. Consequently, shorter liquid slugs can strengthen mixing better than longer slugs.

Variations of pressure at the junction (black dot position in Fig. 9) $\tilde{p}_{\text{jun}}$ and gas flow rate $\tilde{Q}_g$ (nondimensionalized by $u_{\text{in}}D_2$) are plotted in Figs. 9 and 10 up to the time instant when the fourth bubble nearly breaks up. Periodic variations of $\tilde{p}_{\text{jun}}$ and $\tilde{Q}_g$ can be observed in this process. Figure 9 also clearly shows the three stages in one bubble

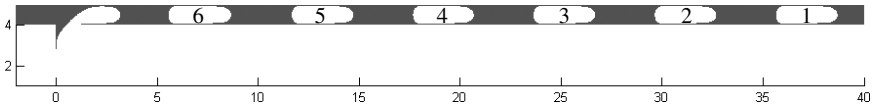


Fig. 5. Simulated bubble sequence snapshot at $\tilde{D}_1 = 1$, $\tilde{W} = 40$, $\tilde{p}_g = 900$, and $Ca = 0.03$.

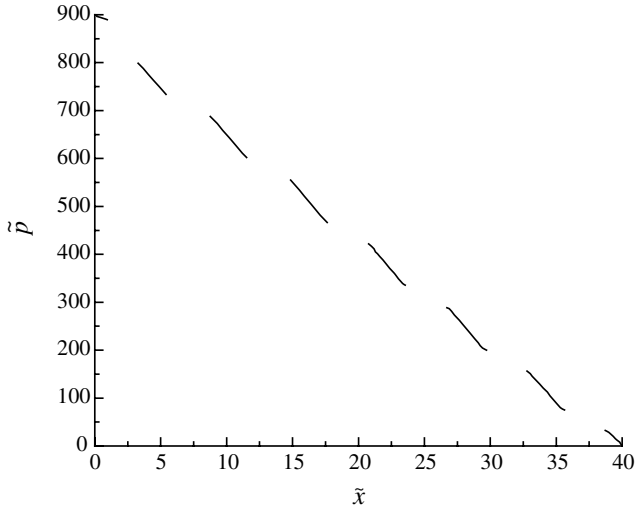


Fig. 6. Pressure distribution in the liquid phase along the centerline of main channel.

formation period: when gas tip is still in the gas channel before entering the main channel, the pressure at the junction is the lowest; with the gas tip gradually blocking the cross-section of main channel, the pressure on the upstream of the growing bubble accumulates to a high value; during the squeezing period, the pressure at the junction keeps high and reaches the highest value when a bubble is just about to break up. After the bubble breaking up, the situation returns to the first stage quickly.

Let $\Delta\tilde{p}_i$ be the pressure drop from the junction to the outlet when the $i$th bubble is generated and there are $(i-1)$ bubbles in the main channel if the first bubble has not reached the outlet. It can be calculated based on the pressure drop for Poiseuille flow and the pressure drop across

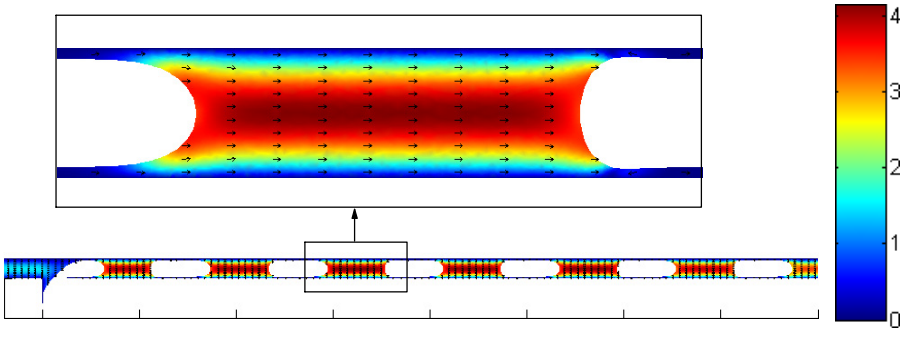


Fig. 7. Absolute velocity field in liquid slugs (color online).

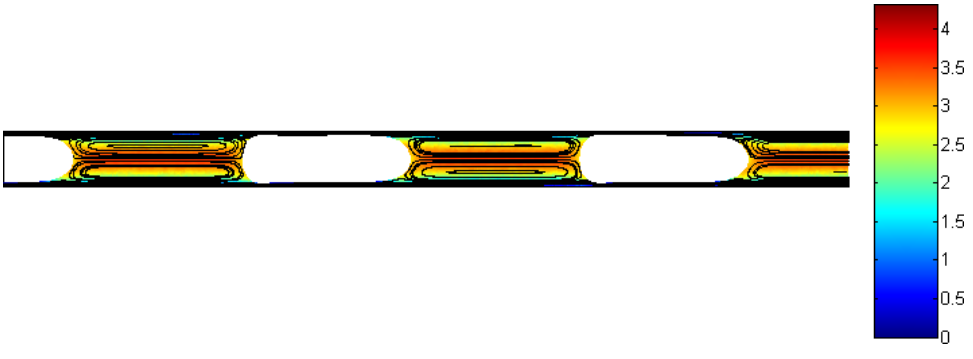


Fig. 8. Streamlines of relative velocity field in liquid slugs (color online).

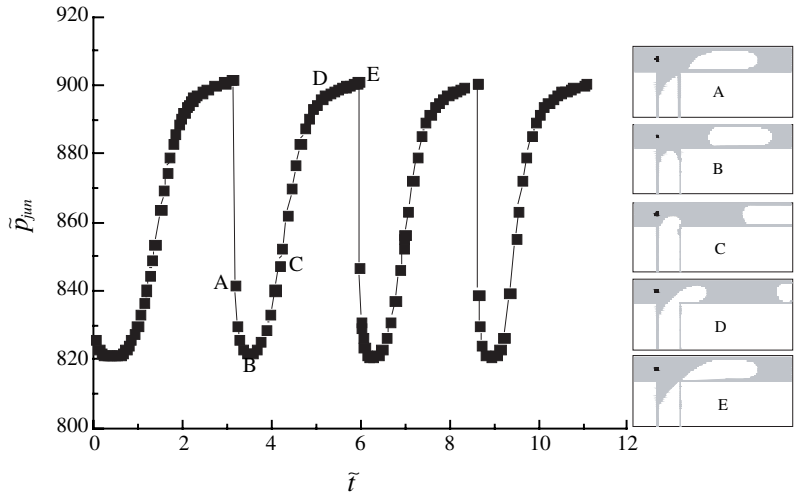


Fig. 9. Variation of the nondimensional pressure at the junction up to the instant when the fourth bubble nearly breaks up (A, B, C, D and E are five typical moments in one bubble formation period).

bubbles:

$$\Delta\tilde{p}_i = 12[\tilde{W} - \tilde{D}_1 - (i-1)\tilde{L}_{\text{bub}}]\tilde{u}_l + (i-1)\Delta\tilde{p}_b\,. \tag{11}$$

Here, $\tilde{u}_l$ is the cross-sectional average velocity of liquid. The pressure drop $\Delta\tilde{p}_b$ across a bubble in circular and 2D capillaries can be evaluated by[27,28]:

$$\Delta\tilde{p}_b = \frac{c}{Ca^{1/3}}\tilde{u}_b^{2/3}\,, \tag{12}$$

where $c$ is a constant of order 10 available in Refs. 29 and 30. Since $Ca$ is usually small for microfluidic systems, $\tilde{u}_b$ and $\tilde{u}_l$ are equal with each other.[27,29,30] Therefore,

$$\Delta\tilde{p}_i - \Delta\tilde{p}_{i-1} = \frac{c}{Ca^{1/3}}\tilde{u}_b^{2/3} - 12\tilde{L}_{\text{bub}}\tilde{u}_l\,. \tag{13}$$

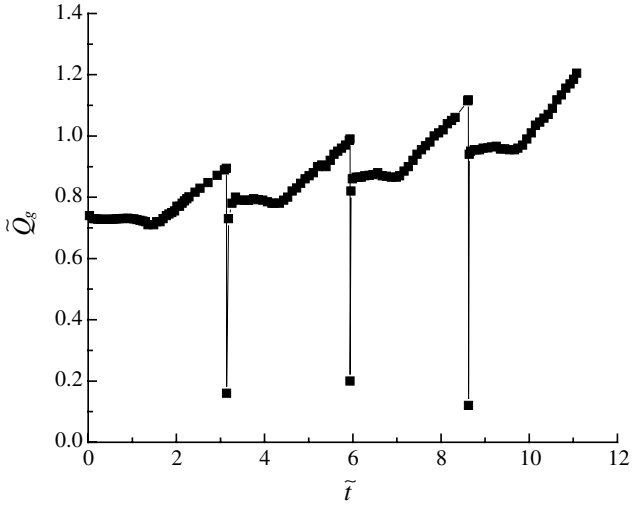


Fig. 10. Variation of the nondimensional gas flow rate up to the instant when the fourth bubble nearly breaks up.

If $(\Delta\tilde{p}_i - \Delta\tilde{p}_{i-1})$ is smaller than 0, such as the case in Fig. 5, the size of the $i$th bubble is larger than that of the $(i-1)$th bubble. If $(\Delta\tilde{p}_i - \Delta\tilde{p}_{i-1})$ is larger than 0, which is likely to occur at small $Ca$ and small $\tilde{L}_{\text{bub}}$, the $i$th bubble is smaller than the $(i-1)$th bubble. If $(\Delta\tilde{p}_i - \Delta\tilde{p}_{i-1})$ equals to 0, the sizes of the $i$th and $(i-1)$th bubble are expected to equal with each other. Therefore, the variation of bubble size before the first bubble reaches the outlet can be controlled by adjusting the sign of $(\Delta\tilde{p}_i - \Delta\tilde{p}_{i-1})$. For a fixed operational condition, the bubble size will become constant soon after the first bubble leaves the system.[17,18]

### 3.2. *Impact of channel width ratio on the final bubble-based two-phase flow*

For the purpose of either producing nanoliter-bubbles or strengthening liquid mixing by using microfluidic T-junctions, shorter bubbles and shorter liquid slugs are preferable. We conduct the following analyses based on small $Ca$ assumption to show how channel width ratio influences the bubble formation process.

Note that bubbles flow at the same velocity as the surrounding liquid when $Ca$ is very small. The total nondimensional bubble length can be calculated by:

$$\tilde{L}_{\sum \text{bub}} = \frac{\tilde{W}\tilde{Q}_g}{1+\tilde{Q}_g}\,. \tag{14}$$

According to the scaling in Ref. 31 and the modification in Ref. 16, the length of one bubble can be

predicted by:

$$\tilde{L}_{\text{bub}} = \tilde{D}_1 \tilde{Q}_g + 1\,. \tag{15}$$

We can thus approximate the number of bubbles in the main channel at the steady state:

$$n = \frac{\tilde{L}_{\sum \text{bub}}}{\tilde{L}_{\text{bub}}} = \frac{\tilde{W}\tilde{Q}_g}{(1+\tilde{Q}_g)(\tilde{D}_1\tilde{Q}_g + 1)}\,. \tag{16}$$

It shows that when

$$\tilde{Q}_g = \sqrt{1/\tilde{D}_1}\,, \tag{17}$$

$n$ has a maximum value. This phenomenon is demonstrated in Fig. 11(a). In other words, for certain geometry and fluids, when nondimensional gas flow rate fulfills Eq. (17), the total nondimensional length of a bubble and a liquid slug is the smallest, or there are the most bubbles existing in the main channel at the same time. Figure 11(b) demonstrates the maximum-$n$-condition of the gas–liquid two phase flow for three geometries with the same main channel width, the same liquid inlet flow rate, as well as the same fluid properties, but with three different gas channel widths $\tilde{D}_1$. According to Eqs. (15) and (17), the bubble length equals to $\sqrt{\tilde{D}_1} + 1$. Therefore, bubbles are the smallest at $\tilde{D}_1 = 0.25$; at the same time, the liquid slugs are the shortest. Moreover, according to the following relation regarding bubble formation time,

$$\tilde{t} = \frac{\tilde{V}_{\text{bub}}}{\tilde{Q}_g} \cong \frac{\sqrt{\tilde{D}_1} + 1}{\sqrt{1/\tilde{D}_1}}\,, \tag{18}$$

where $\tilde{V}_{\text{bub}}$ characterizes the bubble size, bubbles are also generated at a fastest rate for the smallest $\tilde{D}_1$. For the purpose of using microfluidic T-junction as a bubble-generation device, small $\tilde{D}_1$ T-junctions can generate smaller bubbles with a faster speed. For the purpose of improving chemical reaction, small $\tilde{D}_1$ T-junctions more enhance the mixing within liquid phase due to the shorter liquid slugs. To obtain the same short liquid slugs in a T-junction with larger $\tilde{D}_1$, the bubbles will be much longer.

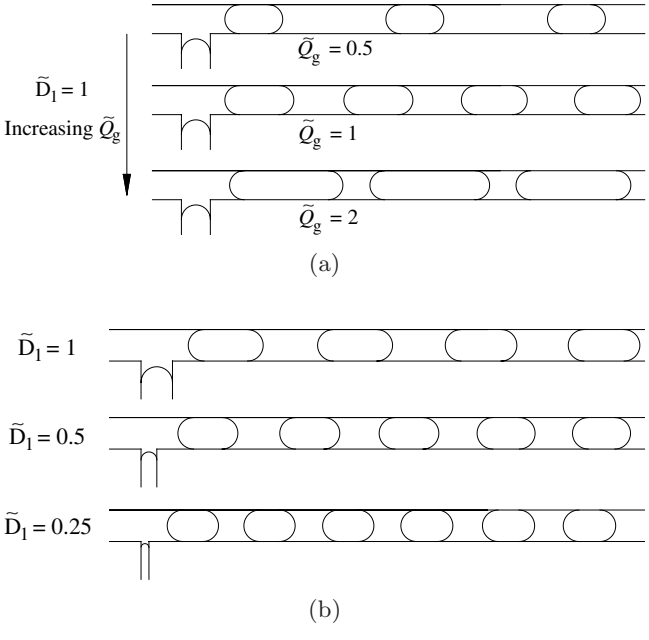


Fig. 11. (a) Change of bubble and liquid slug lengths with increasing gas flow rate. (b) Change of bubble and liquid slug lengths with different gas channel widths for the case when there is maximum number of bubbles in the main channel.

### 3.3. *Minimum gas pressure*

Both simulations and experiments show that for fixed T-junction geometry, fluid properties and liquid inlet flow rate, bubbles can be generated only when the gas pressure is higher than a critical value.[17,18] This inspires us to find the minimum value of nondimensional gas pressure $\tilde{p}_{g\,\text{min}}$ for generating bubbles. Since the volume flow rate at the outlet equals the total inlet flow rates of liquid and gas for incompressible fluids, and the minimum gas pressure corresponds to almost zero gas flow rate, the volume flow rate at the outlet should be almost equal to but slightly larger than the inlet volume flow rate of liquid. Therefore, there are few bubbles in the main channel, so that the flow rate at the outlet $Q_{\text{out}}$ can be calculated based on the Poiseuille flow:

$$Q_{\text{out}} = \frac{D_2^3}{12\mu} G\,, \tag{19}$$

where $G$ is the pressure gradient and can be approximated by the pressure drop from the junction to the outlet divided by $W$. Both simulation and experiment shows that after a bubble breaks up from the gas stream, the residual gas tip changes from an angular shape to a roundish one (Fig. 3). For smaller gas pressure, the gas tip is more likely to become a semicircle shape in the gas channel before entering the main channel and deflecting with liquid. For the case of minimum gas pressure, the liquid pressure near the semicircle gas tip is thus approximately $p_g - 2\gamma/D_1$. Noting that the superficial liquid pressure at the outlet is zero, we have

$$G = \frac{p_g - 2\gamma/D_1}{W}\,. \tag{20}$$

Therefore,

$$Q_{\text{out}} = \frac{D_2^3}{12\mu}\frac{p_g - 2\gamma/D_1}{W}\,. \tag{21}$$

The nondimensional outlet flow rate is

$$\tilde{Q}_{\text{out}} = \frac{Q_{\text{out}}}{u_{\text{in}}D_2} = \frac{1}{12}\frac{\tilde{p}_g - (2/Ca\cdot\tilde{D}_1)}{\tilde{W}}\,. \tag{22}$$

Note that the inlet flow rate is nondimensionalized as $\tilde{Q}_{\text{in}} = Q_{\text{in}}/u_{\text{in}}D_2 = 1$. For generating bubbles, we require

$$\frac{1}{12}\frac{\tilde{p}_g - (2/Ca\cdot\tilde{D}_1)}{\tilde{W}} > 1 \tag{23}$$

or

$$\tilde{p}_g > \tilde{p}_{g\,\min}\,, \tag{24}$$

where the minimum gas pressure

$$\tilde{p}_{g\,\min} = 12\tilde{W} + \frac{2}{Ca\cdot\tilde{D}_1}\,. \tag{25}$$

In order to generate a bubble, therefore, the gas pressure must be large enough to overcome the flow resistance in the downstream section and the pressure difference between two phases due to the interfacial tension.

## 4. Concluding Remarks

The Runge–Kutta finite element method is successfully implemented to simulate the nanoliter-bubble formation process in microfluidic T-junctions for the Stokes flow regime. The simulated pressure distribution and velocity field indicate the flow in liquid slugs between bubbles is Poiseuille flow except the regions near bubble caps. Vortexes are observed for the relative velocity of liquid to bubbles. The mixing of liquid can thus be enhanced, especially for shorter liquid slugs, in such bubble-based flow system. Secondly, the sizes of the first several bubbles tend to increase for relatively large $Ca$ value and large bubbles, and decrease for small $Ca$ and small bubbles. Thirdly, for the same liquid inlet flow rate and main channel width, smaller gas channel can produce both shorter bubbles and shorter liquid slugs at a faster speed. Thus T-junction with small channel width ratio between the gas channel and the main channel is preferable for either producing nanoliter-bubbles or enhancing mixing within the liquid phase. Finally, we obtain the critical value of nondimensional gas pressure above which bubbles can be generated.

## Acknowledgments

The financial support from the Research Grants Council of Hong Kong (GRF718009) and the CRCG of the University of Hong Kong (200707176111) is gratefully acknowledged.

## References

1. S. S. Sadhal, P. S. Ayyaswamy and J. N. Chung, *Transport Phenomena with Drops and Bubbles* (Springer, New York, 1997).
2. M. Sommerfeld, *Bubbly Flows* (Springer, New York, 2004).
3. H. C. Chang, Bubble/drop transport in microchannels, *The MEMS Handbook: Introduction and Fundamentals*, ed. M. Gad-el-Hak (Taylor and Francis, Boca Raton, 2006), pp. 1–13.
4. A. M. Gañán-Calvo and J. M. Gordillo, *Phys. Rev. Lett.* **87**, 274501 (2001).
5. A. Terfort, N. Bowden and G. M. Whitesides, *Nature* **386**, 162 (1997).
6. M. Srinivasarao, D. Collings, A. Philips and S. Patel, *Science* **292**, 79 (2001).
7. S. S. Jenekhe and X. L. Chen, *Science* **283**, 372 (1999).
8. E. Winfree, F. R. Liu, L. A. Wenzler and N. C. Seeman, *Nature* **394**, 539 (1998).
9. P. Marmottant and S. Hilgenfeldt, *Nature* **423**, 153 (2003).
10. P. Yager, T. Edwards, E. Fu, K. Helton, K. Nelson, M. R. Tam and B. H. Weigl, *Nature* **442**, 412 (2006).
11. M. Lundh, L. Jonsson and J. Dahlquist, *Water Res.* **34**, 21 (2000).
12. P. Garsteck, M. J. Fuerstman, M. A. Fischbach, S. K. Sia and G. M. Whitesides, *Lab Chip* **6**, 207 (2006).
13. S. B. Feinstein, *Am. J. Physiol. Heat Circ. Physiol.* **287**, H450 (2004).
14. E. C. Unger, E. Hersh, M. Vannan, T. O. Matsunaga and T. McCreery, *Prog. Cardiovasc. Dis.* **44**, 45 (2001).
15. J. H. Xu, S. W. Li, Y. J. Wang and G. S. Luo, *Appl. Phys. Lett.* **88**, 133506 (2006).
16. V. van Steijn, M. T. Kreutzer and C. R. Kleijn, *Chem. Eng. Sci.* **62**, 7505 (2007).
17. Y. X. Zhang and L. Q. Wang, *Nanoscale Microscale Thermophys. Eng.* **13**, 228 (2009).
18. L. Q. Wang, Y. X. Zhang and L. Cheng, *Chaos Sol. Frac.* **39**, 1530 (2009).
19. P. Garstechi, M. A. Fischbach and G. M. Whitesides, *Appl. Phys. Lett.* **86**, 244108 (2005).
20. A. Gunther, S. A. Khan, M. Thalmann, F. Trachsel and K. F. Jensen, *Lab Chip* **4**, 278 (2004).
21. F. Guo and B. Chen, *Micrograv. Sci. Tech.* **21**, S51 (2009).

22. D. Y. Qian and A. Lawal, *Chem. Eng. Sci.* **61**, 7609 (2006).
23. R. Gupta, D. F. Fletcher and B. S. Haynes, *Chem. Eng. Sci.* **64**, 2941 (2009).
24. M. J. Jensen, H. A. Stone and H. Bruus, *Phys. Fluids* **18**, 077103 (2006).
25. M. J. Jensen, PhD thesis, Technical University of Denmark (2006).
26. COMSOL AB. COMSOL Multiphysics User's Guide. COMSOL 3.5a (2008).
27. H. Wong, C. J. Radke and S. Morris, *J. Fluid Mech.* **292**, 95 (1995).
28. M. J. Fuerstman, A. Lai, M. E. Thurlow, S. S. Shevkoplyas, H. A. Stone and G. M. Whitesides, *Lab Chip* **7**, 1479 (2007).
29. H. Wong, C. J. Radke and S. Morris, *J. Fluid Mech.* **292**, 71 (1995).
30. L. W. Schwartz, H. M. Princen and A. D. Kiss, *J. Fluid Mech.* **172**, 259 (1986).
31. P. Garstecki, M. J. Fuerstman, H. A. Stone and G. M. Whitesides, *Lab Chip* **6**, 437 (2006).